Study and characterization of optical materials and gas mixtures of advanced tunable pulsed lasers in the UV and in the visible spectral region

A. Papayannis (Scientific Coordinator, Assist. Professor), A. A. Serafetinides (Principal Researcher, Professor), M. Makropoulou (Researcher, Assist. Professor), D. Papadopoulos (Researcher, PhD student), A. Papagiakoumou (Researcher, PhD student), G. Chourdakis (Researcher, PhD student), G. Georgoussis (Post-doc Fellow), B. Klinkenberg (Researcher, Graduate student)

Laboratory of Lasers and their Applications, Department of Physics,
National Technical University of Athens, Zografou Campus, Greece

Introduction

The main objectives of this project were: a) the spectroscopic investigation of the Ce:LiSAlF crystal using the EPR (Electronic Paramagnetic Resonance) and the Raman technique, b) the study of various parameters of gas mixtures in a high-pressure Raman cell, c) the optical pumping of a Ce:LiSAlF crystal by the 4^{rth} harmonic (266 nm) of a pulsed Nd:YAG laser, and d) the investigation of pulsed UV laser light propagation in optical fibres. All these experiments were carried out in order to find the optimum conditions to obtain suitable coherent light beams in the UV-VIS spectral region, which could be used as laser sources for environmental, medical and industrial applications.

1. Spectroscopic study of Ce:LISAlF crystals

$LiSrAlF_6$ (LiSAF) crystals doped with Ce^{+3} have recently attracted much interest as laser gain materials, with potential use in various medical, industrial, environmental, and many other scientific applications. Undoped and Ce-doped LiSAF crystals have been grown using the Czochralski method. Cerium was co doped with sodium with concentrations of 0.5 mol% in the starting material. The final concentration is anticipated to approximately 0.007 mol% for Ce and 0.02 mol% for Na (Ruiz et al., 2002).

Characteristic Electron Spin Resonance (ESR) spectra of the Ce:Na:LiSAF crystal, measured at different angles ω, are shown in Fig. 1. For ω near 0° and 180°, three different peaks are clearly observed in the spectra. To the contrary, for the intermediate angles ω, the ESR spectra are rich of resonance lines: the maximum number of peaks and the broader resonance field range were observed for angles near 90°. All these peaks are interpreted as being due to Ce atoms in different crystalline environments due to the presence of Na charge compensators at different relative distances. The various peaks, *A*, *B*, *C*, and *D*, correspond to different Na positions according to the interpretation referred to in the following section. While the strong *A* resonance dominates all spectra with a single line, the *B* and *D* resonances are split in two lines having a ratio of about 1:2 and superimposed onto one line for angles adjacent to 0°. The 1, 2, or 3 multiplicity of the *B* and *D* lines is marked in Fig. 1 by a corresponding superscript index. The most intense satellite *B* and *C* lines can be identified in all the spectra and have a ratio of about 3:1. The above mentioned intensity ratios are more or less preserved for all the different angles and they are used as a criterion for the identification of the different resonances. The ω dependence of the various resonance lines has been grouped in plots (a) and (b) of Fig. 2 for the *A* and *B* resonances and plots (a) and (b) of Fig. 3 for the *C* and *D* ones, respectively.

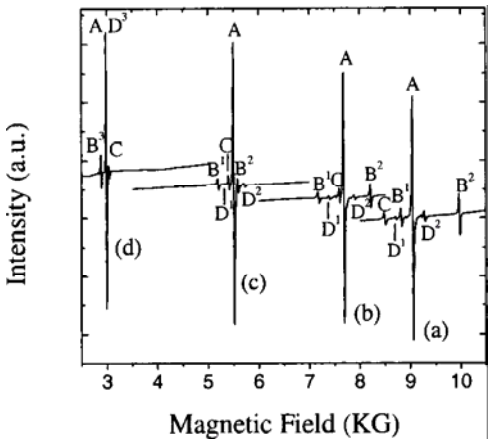

FIG. 1. Characteristic ESR spectra taken at 11 K, with the magnetic field in the *a*–*c* plane at four different angles v with reference to the *c* axis: (a) 92.5°, (b) 102.5°, (c) 117.5°, and (d) 184°. The spectra have been shifted vertically for clarity. Different resonance lines have been attributed to different local crystalline environments of the Ce atoms. The superscript index indicates degeneracy of resonances *B* and *D* into one, two, or three lines.

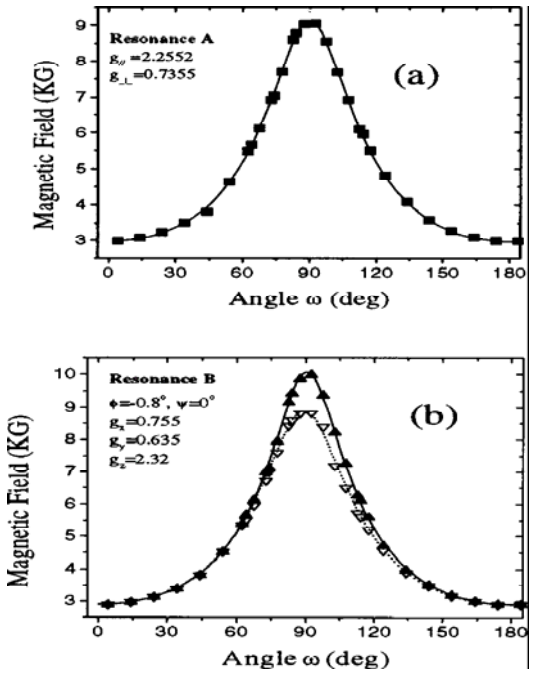

FIG. 2. (a) The dependence of the *A* ESR resonance peak position vs the angle ω between the direction of the *c* axis and that of the external magnetic field. The fitting curve considers an axial *g* tensor. (b) The same for the *B* resonance. In this case the fitting is done with a rhombic *g* tensor. The solid (open) symbols correspond to the doubly (singly) degenerate line, respectively.

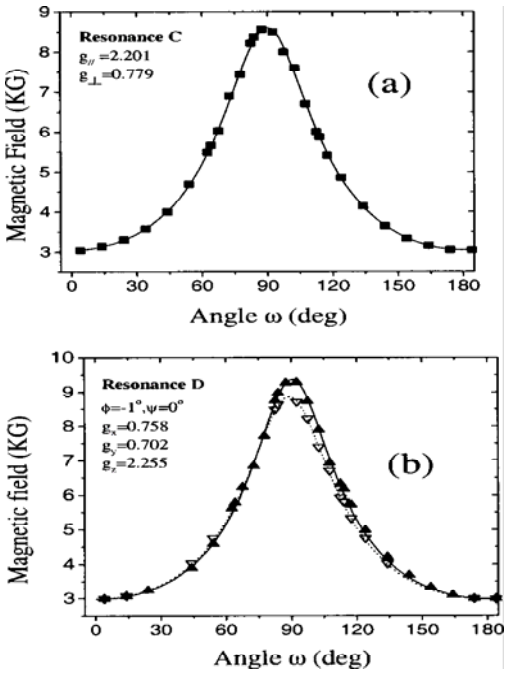

FIG. 3. The angle dependence of the ESR resonance lines, which were assigned to the axially symmetric *C* resonance (a) and the orthorhombic one *D*. (b) The solid (open) symbols stand for the doubly (singly) degenerate line, respectively. The solid lines are fittings taking an axial (a) and a rhombic (b) *g* tensor, correspondingly.

In Fig. 4 we have plotted the linewidth ΔH of the main resonance *A* line relative to the absolute temperature *T*. An exponential increase of ΔH upon increasing *T* is observed, which suggests the Orbach process as the dominant spin lattice relaxation mechanism (Orton 1968; Abragam et al., 1986).

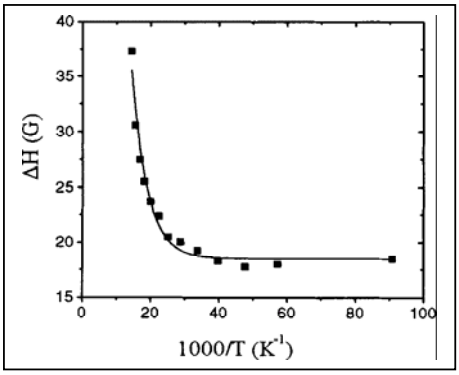

FIG. 4. The inverse temperature dependence of the main ESR resonance linewidth, undertaken with *B* parallel to the *c* axis.

Accordingly we get $\Delta H = \alpha + b\exp\left(-\frac{\Delta E}{\kappa_\beta T}\right)$ (1), where *kB* is the Boltzman constant and ΔE is the energy difference between the ground and the first excited electronic state. A substitution of our data to (1) results in ΔE=149±5 cm^{-1}, with fitting parameters *a*=18.6±0.5 G and *b*=376±50 G. The resonance position of the most intense *A* peak in the ESR spectra Fig. 2(a) presents an angular dependence with an axially symmetric effective $g(\omega)$ tensor defined as $g(\omega) = \left(g_{//}^2 \cos^2\omega + g_\perp^2 \sin^2\omega\right)^{\frac{1}{2}}$. By fitting our experimental data to the above equation we get $g_{//}$=2.255±0.004 and $g_\perp$=0.735±0.005. The excellent fitting of the *A* line to Eq. (1) shows that the *A*-type Ce site preserves a trigonal symmetry. This indicates that Ce, in this case, is quite isolated from nearby Na^+ ions. For illustrative purposes, a LiSAF unit cell, which hosts a Ce^{3+} ion at a Sr^{2+} site, has been drawn in Fig. 6(a), where the *A* position of a Na^+ charge compensating ion in a far distance is marked. The behavior of the resonance site *B* in Fig. 1 suggests a Ce lattice site with orthorhombic symmetry. Considering the orthorhombic environment as a superposition of the initial distorted along the-*c* octahedral system (*abc*) with another axially symmetric distortion (along an arbitrary *c*′), the final biaxial *g* tensor ellipsoid has its two principal axes on the *c* – *c*8 plane. Therefore, the orthorhombic system *xyz* can be defined with respect to *abc* with two angles, as shown in Figs. 5a and 5b, where, φ is the angle between *c* and *z* and ψ is the angle between *a* and the projection of *z* to the *a* – *b* plane. Raman spectra were recorded (Fig. 6) with incident and scattered light parallel to the *c* and *a* axis, in all possible combinations (*a*-*a*, *c*-*c*, *a*-*c*). All samples, including that of the undoped reference, show the same Raman modes without any remarkable differences.

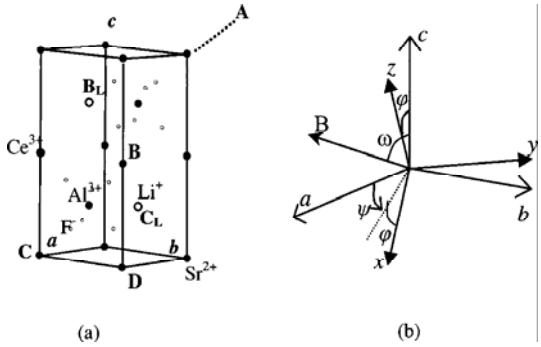

FIG. 5. (a) A schematic diagram of the $LiSrAlF_6$ crystal structure. *A* label indicates a Na atom lying far from the Ce dopant position. *B*, *C*, and *D* labels show the Na^+ sites up to third neighbors to a Ce dopant. B_L and C_L stand for the first and second neighbors to the Ce lattice sites of Li^+ vacancies. (b) A drawing of the principal crystalline axes system, where the magnetic field is in the *c* – *a* plane and points at an angle v to the *c* axis. The transformation of the axes is shown for an orthorhombic environment at arbitrary angles φ and ψ relative to the principal axes system.

Conclusions

ESR measurements of Ce doped LiSrAlF6 single crystals have shown that Ce resides mainly in an axially symmetric Sr position. The effective *g* factor of this Ce resonance has been

determined and conclusions have been drawn for the electronic eigenfunctions, which describe the ground state energy level. Ce resonances due to Ce sites with orthorhombic symmetry have been detected in the ESR spectra with multiple lines.

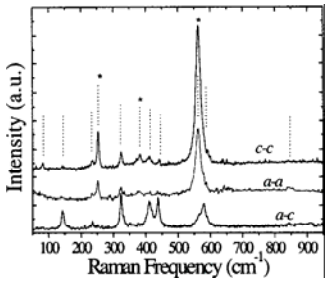

FIG. 6. The Raman spectra of the undoped LiSAF crystal recorded with parallel *c-c* and *a-a* and crossed *a-c* polarizations of the incident and scattered beams. The observed bands are marked with vertical lines. The bands that are substantially reduced in the *a-c* configuration are marked by stars.

These resonances have been attributed to charge compensating Na1 ions, which perturb the crystal field environment at Ce sites in the direction of the Sr–Sr bonds. ESR resonances, which result from up to the third neighbouring Na to Ce sites, have been identified and the principal values of the corresponding *g* tensors have been estimated. Nonetheless, the crystal field distortion in the *c* axis remains the dominant one and determines, by a maximum deviation of 1°, the one principal axis direction of the *g* tensor. The effective *g* factor of these resonances as well as the Na1 occupation sites and probabilities have been estimated and are further correlated to the material lasing properties, always in comparison to the isostructural LiCaAlF6 . The energy splitting between the ground and the first excited electronic states has been estimated by the temperature dependence of the ESR linewidths. Undoped as well as Cr and Ce doped LiSAF crystals were further examined for their lattice dynamical properties. Polarized Raman measurements have been combined with group theoretical arguments in order to identify the observed lattice vibrational modes. Strain or disorder effects were not detected in the Raman spectra (Kontos et al., 2003).

2. Study of gas mixture in a Raman cell

Measurements of the concentration of aerosols and other molecular atmospheric pollutants using the LIDAR – DIAL (Differential Absorption LIDAR) techniques are of great interest. These techniques provide the ability of estimating the vertical profile of the concentration of various atmospheric pollutants with very high spatial and temporal resolution. One of the main air pollutants is ozone (O_3) mostly produced photochemically in the Planetary Boundary Layer (PBL). Recently, several DIAL systems have been developed to measure tropospheric ozone in the atmosphere, using laser sources emitting in the UV spectral region (Papayannis et al., 1990; de Tomasi et al., 2001). The wavelengths of interest for ozone measurements in the PBL are in the UV spectral region (280-320 nm). Wavelengths in this region are obtained if a Raman cell filled with H_2, D_2 or mixture of them is optically pumped by the 4^{th} harmonic of a Nd:YAG laser (266 nm). This procedure is called stimulated Raman scattering effect (SRS).

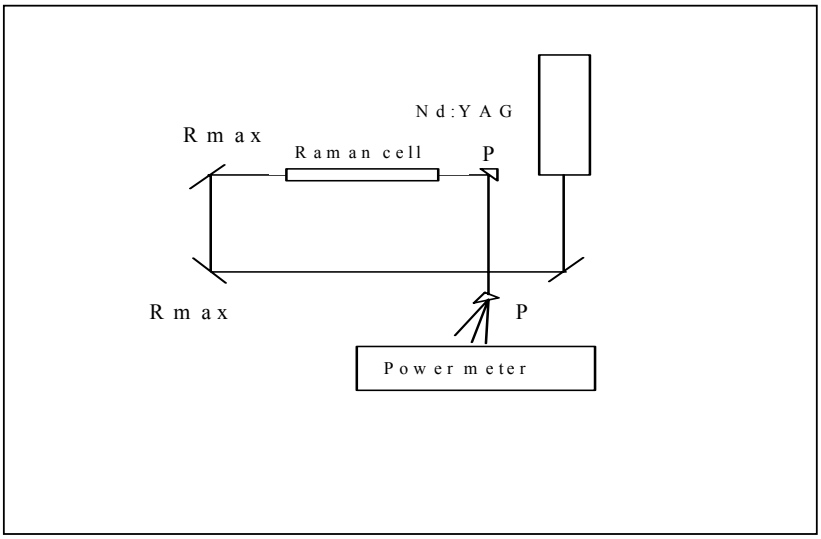

Fig. 7. The SRS experimental setup.

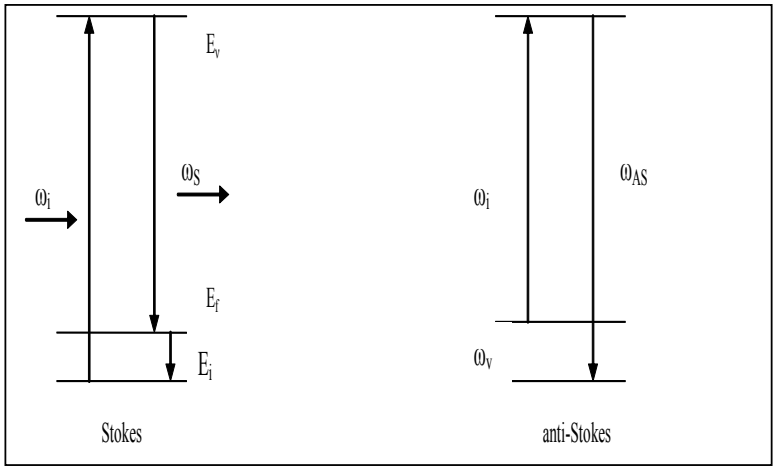

Fig. 8 The Raman scattering effect.

In the frame of this project a 60 cm long Raman cell was optical pumped having 30 mm diameter quartz lenses as windows. The laser pump energy (at 266 nm) was11±1 mJ per pulse and the repetition rate was 10 Hz. In Fig. 7 the experimental setup is presented. Three dichroic mirrors (R_{max} = 98.5% at 266 nm) were used so that the beam is purified from the 1064 nm and 532 nm, components, both emitted by the Nd:YAG laser. Two prisms were engaged in order to separate the outgoing wavelengths. The SRS procedure is presented in Fig. 8. Several experiments were performed to estimate the conversion efficiencies of the SRS effect for H_2, D_2 at different pressures and mixture (H_2+D_2) of different proportions inside the Raman cell. The results are presented in Fig. 9 (a),(b), (c). The losses in the Raman cell due to absorption and scattering procedures are estimated to be approximately 6.6% and were taken into consideration for the proper calculations of the resulting conversion efficiencies.

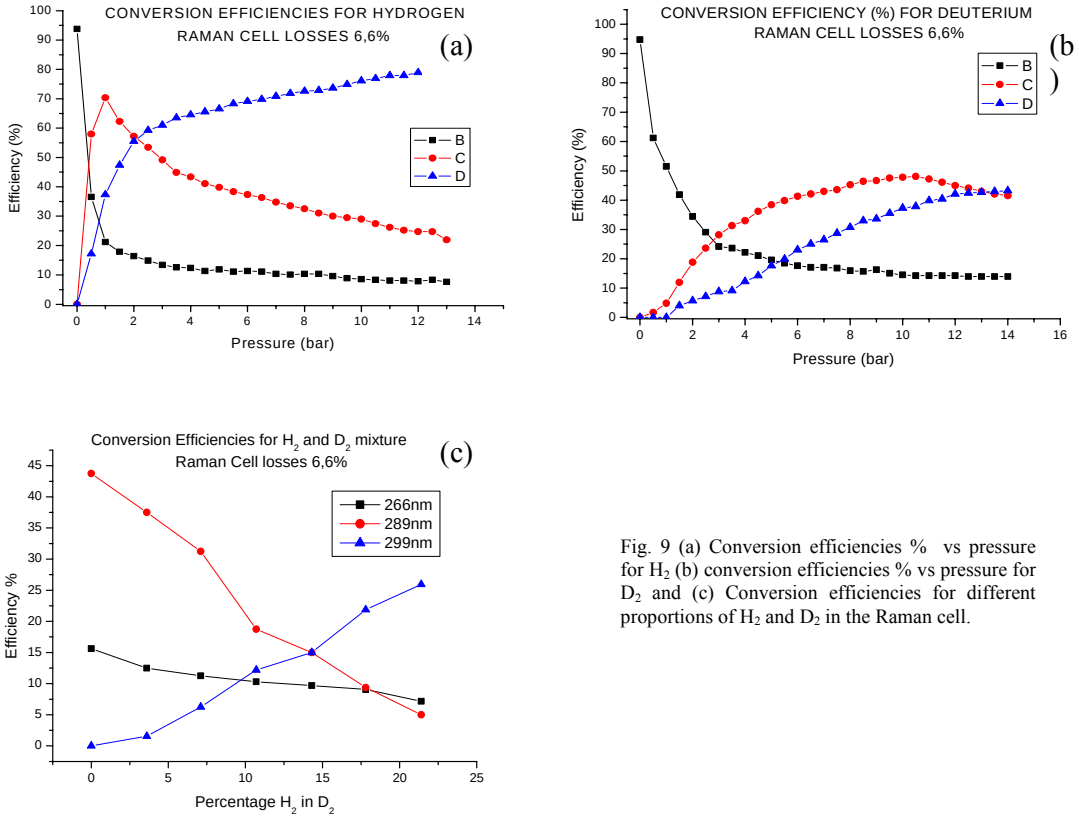

Fig. 9 (a) Conversion efficiencies % vs pressure for H_2 (b) conversion efficiencies % vs pressure for D_2 and (c) Conversion efficiencies for different proportions of H_2 and D_2 in the Raman cell.

Conclusions

Hydrogen presents higher conversion efficiencies compared to D_2 (Schoulepnikoff et al., 1997) due to its higher gain coefficients. Thus, the maximum efficiency (70%) for H_2 was found at 1 bar pressure, while for pressures above 2 bar the 2nd stokes (341 nm) is optimized. Maximum efficiency (48%) for D_2 appeared at 10.5 bar pressure. We could not get satisfactory results for the 2nd stokes of D_2 (314 nm) due to system limitations in pressure values lower than 14 bar. Based on the results obtained for single H_2 and D_2 gases, we used a mixture of these two gases, as an active gas. The percentage of H_2 in the mixture varied from 0 – 21.5%. For 14.3% H_2 (H_2:D_2=1:6 i.e. 2 bar H_2 and 12 bar D_2 the efficiencies are the same with a value of 15%. The divergences of the emitted beams were also measured and found to be approximately 2.2 mrad much higher (as expected) than the divergence of the pumping beam (266 nm), which is of the order of 0.5 mrad.

3. Optical pumping of Ce:LiSAlf crystal using the 4rth harmonic (266nm) of an Nd:YAG Laser

A simple UV – VIS laser cavity was used for the optical pumping of a Ce:LiSAlF (0.1% mol) crystal, directly from the 4th harmonic (266 nm, 10±1 mJ per pulse, 6 ns) of a Nd:YAG laser. The crystal was grown in IPEN Laboratories (Brazil). Two of its sides were polished in order to be used for laser activity. The total absorption of the crystal at 266nm is 10^{-4} cm^{-1}. In Fig 10 a schematic representation of the laser cavity used for the pumping of the sample is shown. The first mirror (K_1) was Cr coated with 100% reflectivity while the second

(output coupler) (K_2) was also Cr coated (coating thickness 200Å) and was of 10% transmittance (high–Q cavity). A quartz lens was used to focus the pumping bean in a spot of 1.5 mm diameter, 5 cm before the crystal. The alignment of the cavity was performed with a He – Ne laser. Unfortunately no output laser beam was observed. This was attributed to the high – Q cavity and to the low energy of the pumping beam. To obtain output energy of the order of mJ a pumping beam with energy 30 – 50 mJ and an output coupler with 40 – 50% transmittance should be used. Experiments were carried out using an output coupler with 45% transmittance at 285 – 289nm (Cr coating of 75Å thickness) yet no output laser beam was obtained. So we concluded that a more powerful pumping bean was needed. We avoided pumping the crystal using flash lamps because due to the inhomogeneous heat distribution within the crystal the sample would be destroyed (Rambaldi et al., 1995).

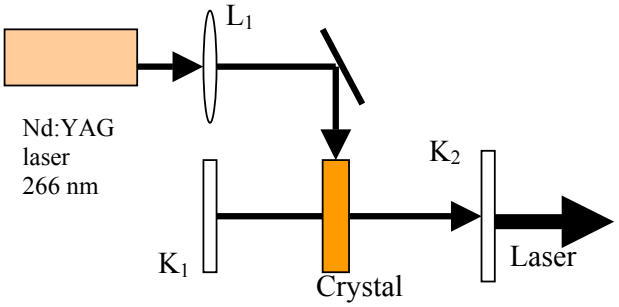

Fig. 10 Laser cavity used to pump a Ce:LiSAlF crystal

4. Investigation of pulsed UV laser light propagation through optical fibres and waveguides

For the study of the UV laser beam propagation in optical fibres and waveguides, the experimental the setups are shown in Figs. 11 (a) and (b), respectively.

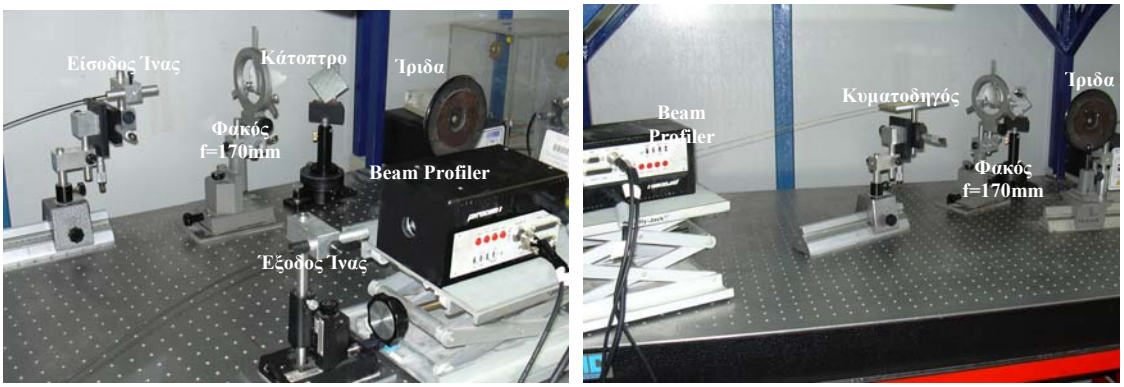

(a) **(b)**

Fig. 11 Setup used for studying the propagation od laser beam through (a) fibre optic, (b) waveguide.

The simultaneously produced wavelengths (355-532 nm) by the Nd:YAG laser were separated using a SiO_2 prism. The beam under investigation (355 nm) was focused with a CaF_2 lens (f = 170 mm) into the fibre/waveguide entrance. The edge of the fibre/waveguide was mounted on a high precision x – y – z mount for optimum coupling of the beam to their entrance. A fused silica fibre with high concentration of OH ions for high transmittance in wide spectral range (from UV to NIR) was evaluated. Its length was 2m, the core diameter was 1.5 mm and the NA = 0.12. The waveguide under investigation was silver hollow glass waveguide with an internal circular olefin coating, length 70 cm and internal diameter of 750 μm. The mean attenuation of the fibre was measured to be 0.45 dB/m or 10% loss/m thus for the waveguide was found 3.3 dB/m or else 54% loss/m. The optical fibre was bended 90^0 and 180^0 and its attenuation was not greatly affected (Gloge, 1972, Papagiakoumou et al., 2003). Similar measurements using the waveguide were not performed because it was not possible to

bend it due to its short length. The spatial profile of the beams was also investigated before and after passing through the fibre/waveguide. The results for the fibre and the waveguide are shown in Figs. 12, 13 respectively. The profile of the beam before entering the fibre/waveguide is of high quality approaching the TEM_{00} mode. The output profile of the beam in the case of the fibre sustains its TEM_{00} character but a more thorough observation reveals the presence of higher order modes underneath the basic TEM_{00}. This is attributed to the manufacturing imperfections of the fibre (Nubling and Harrington, 1997). On the contrary, the waveguide gives out profiles with intense peripheral character. This was also observed in the past when the same waveguide was evaluated at 3 μm and should not be connected to the fact that the 355 nm was far from the optimum wavelength for this waveguide. Probably the generation of higher order modes is because of bad coupling of the beam into the entrance of the waveguide (Nubling and Harrington, 1998).

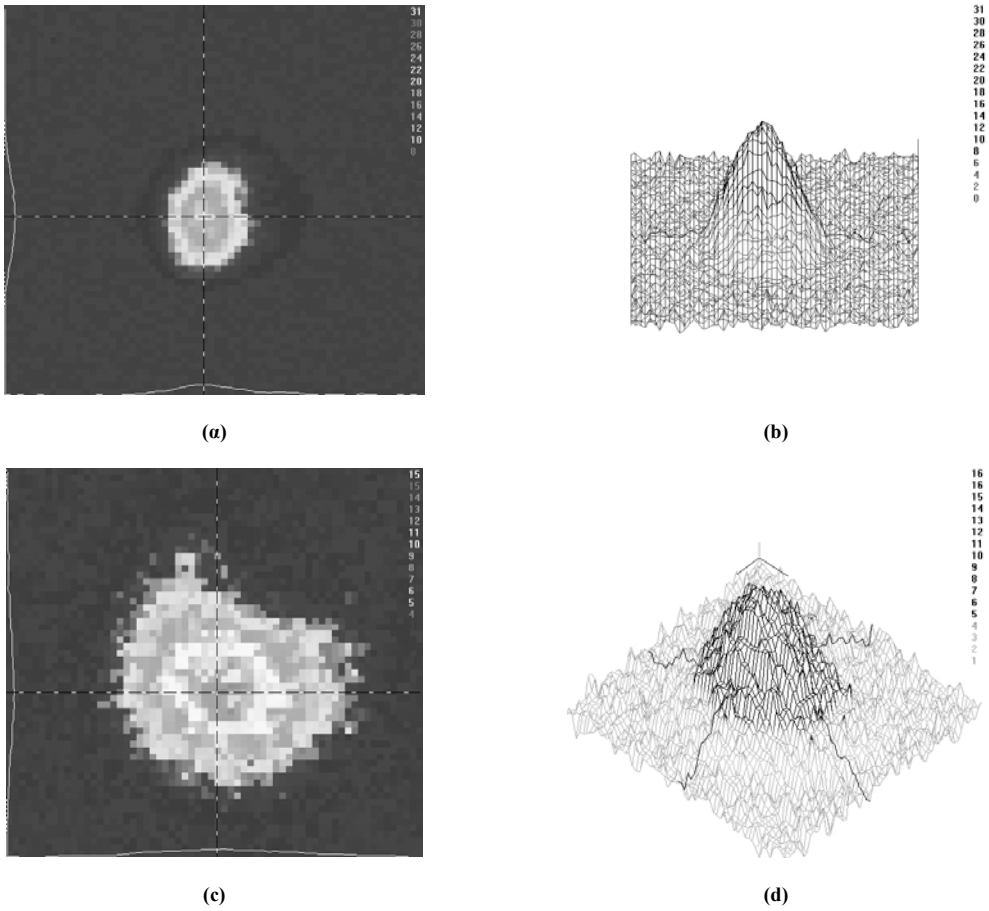

Fig. 12: α,b) The 2D/3D beam profile in the fibre entrance. c,d) To 2D/3D the output beam profile.

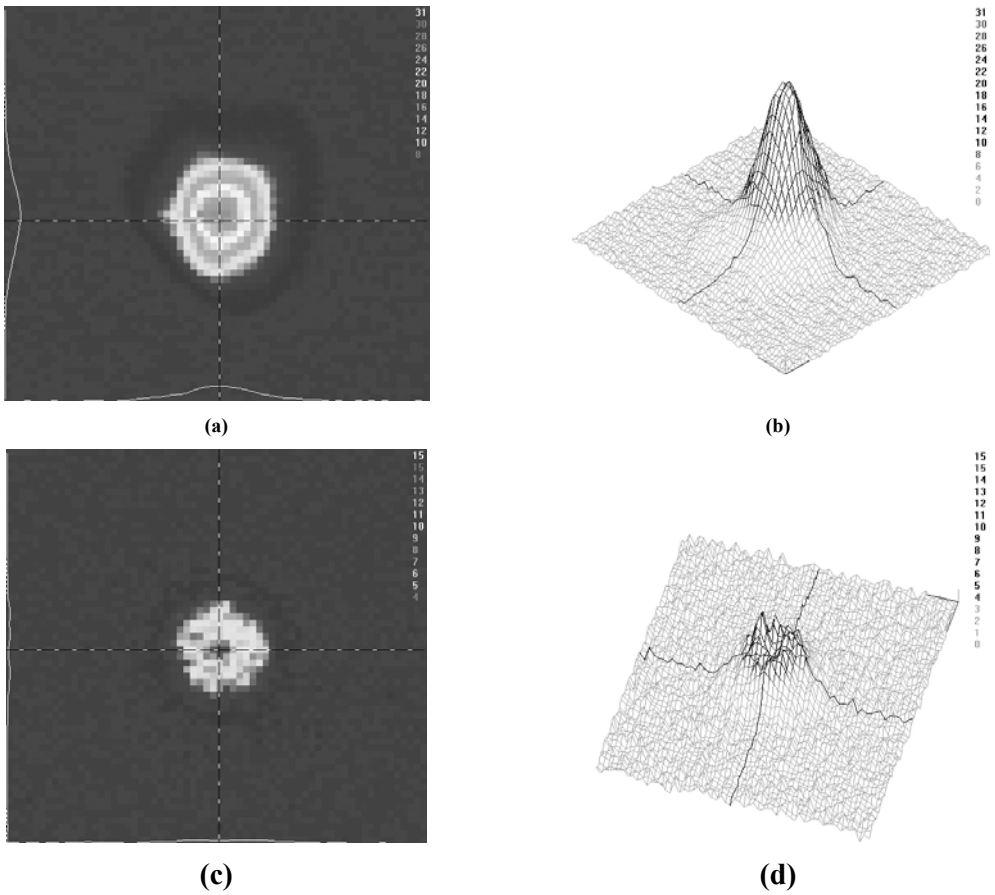

Fig. 13: α,b) The 2D/3D beam profile in the waveguide entrance. c,d) To 2D/3D the output beam profile.

Acknowledgements: This project was financed by the Program for Fundamental Research "**THALIS**" by the National Technical University of Athens, under contract 65/1201 (2002-2004).

References

Abragam, A., and B. Bleaney, *Electron Paramagnetic Resonance of Transition Ions,* Dover Publ., New York, 1986.

De Tomasi, F., M. Perrone, and M. Protopapa, "Monitoring O_3 with solar-blind Raman lidars", *Applied Optics*, **40**, 1314-1320, 2001.

Gloge, D., "Bending loss in multimode fibres with graded and un-graded core index", *Applied Optics*, **11**, 2506-2513, 1972.

Kontos, A.G., G. Tsaknakis, Y. S. Raptis and A. Papayannis, "A Spectroscopic study of Ce- and Cr-doped $LiSrAlF_6$ crystals", *Journal of Applied Physics*, **93**, 2797-2803, 2003.

Nubling, R.K., J.A. Harrington, "Optical properties of single-crystal sapphire fibres", *Applied Optics*, **36**, 5934-5940, 1997.

Nubling, R.K., J.A. Harrington, "Launch conditions and mode coupling in hollow-glass waveguides", *Optical Engineering*, **37**, 2454-2458, 1998.

Orton, J. W., *Electron Paramagnetic Resonance,* Pitman Publ., London, 1968.

Papagiakoumou E., D.N. Papadopoulos, N. Anastasopoulou and A.A. Serafetinides, "Comparative evaluation of HP oxide glass fibres for Q-switched and free-running Er:YAG laser beam propagation", *Optics Communications*, **220**, 151-160, 2003.

Papayannis, A., G. Ancellet, J. Pelon, G. Mégie, "Multiwavelength LIDAR for Ozone Measurements in the Troposphere and the Lower Stratosphere", *Applied Optics,* **29,** 467-476, 1990.

Rambaldi, P., M. Douard, J.-P. Wolf, "New UV tunable solid-state lasers for lidar applications", *Applied Physics B* **61**, 117-120, 1995.

Ruiz, M. C. H. M., E. A. Barbosa, E. P. Maldonado, S. P. Morato, N. U.Wetter, N. D. Vieira, Jr., and S. L. Baldochi, "Zone melting growth of $LiSrAlF_6$:Cr crystals for diode laser pumping", *Journal of Crystal Growth,* **241**, 177, 2002.

Schoulepnikoff, L., V. Mitev, V. Simeonov, B. Calpini and H. van de Bergh, "Experimental investigation of high-power single-pass Raman shifters in the ultraviolet with Nd:YAG and KrF lasers", *Applied Optics*, **36**, 5026-5042, 1997.